CHEMISTRY OF MATERIALS

Cite This: *Chem. Mater.* 2019, 31, 7425−7433

Article

pubs.acs.org/cm

Influence of Anion Charge on Li Ion Diffusion in a New Solid-State Electrolyte, Li_3LaI_6

Zhenming Xu,[∥] Xin Chen,[§] Ke Liu,[∥] Ronghan Chen,[∥] Xiaoqin Zeng,[†,‡,§] and Hong Zhu*[,†,∥]

[†]State Key Laboratory of Metal Matrix Composites, [‡]School of Materials Science and Engineering, and [§]National Engineering Research Center of Light Alloy Net Forming, Shanghai Jiao Tong University, 800 Dongchuan Road, Shanghai 200240, China

[∥]University of Michigan−Shanghai Jiao Tong University Joint Institute, Shanghai Jiao Tong University, 800 Dongchuan Road, Shanghai 200240, China

Supporting Information

ABSTRACT: Based on density functional theory calculations of iodide-type compounds Li_3MI_6 (M = Sc, Y, and La), Li_3LaI_6 with stable octahedral Li occupation is theoretically found to meet the requirements of high lithium ionic conductivity, deformability, and chemical and electrochemical stability simultaneously, which sulfide-type solid-state electrolytes alone have not achieved so far. The underlying mechanism of superior lithium ion conduction in such a halide superionic conductor with stable octahedral Li occupations compared to the spinel ones with tetrahedral Li occupations has been uncovered. The Li migration enthalpies of those materials with face-centered-cubic anion frameworks are found to be not only strongly related to the ratio of anion charge over bond length ($|q_{anion}|/d$) but also dependent on the lithium ion coordination number, which could be a universal design principle for searching new superionic conductors.

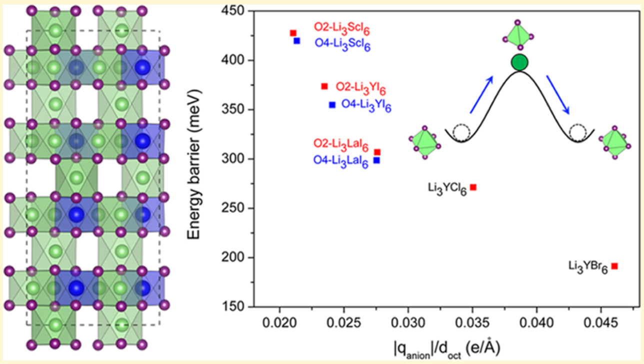

1. INTRODUCTION

As commercial lithium ion batteries (LIBs) approach their theoretical limits for use in large-scale energy storage applications and also face safety issues, replacing the currently employed liquid electrolytes with solid-state electrolytes (SSEs) and matching with Li metal anode to construct all-solid-state lithium ion batteries (ASSLIBs) not only remarkably enhance the energy density of battery system but increase battery safety as well.[1−3] Practical ASSLIBs need SSE materials to achieve fast ion conduction with high Li ionic conductivities (10^{-3}−10^{-2} S/cm) at room temperature. Recent research studies on inorganic superionic conductors have mainly focused on sulfides[4,5] and oxides.[6,7] Sulfide-type lithium ionic conductors, compared to the oxide-type ones, show higher ionic conductivities, deformable mechanical flexibilities to realize intimate interface contacts, and the conveniences of synthesizing by cold-pressing. However, sulfide SSE materials are both chemically and electrochemically unstable,[8,9] which are not only easily oxidized even by dry air but also show frustrating interface compatibilities with $LiCoO_2$ cathode[10] and Li metal anode.[11] On the other hand, oxides are more chemically and electrochemically stable[8,12] compared to sulfides. Nonetheless, oxides also face some obstacles with respect to their practical applications in ASSLIBs, including relatively low ionic conductivities and inferior deformabilities (poor interface contacts with cathodes).[13] It is still full of challenges to develop SSE materials with high ionic conductivities, good deformabilities, and electrochemical stabilities simultaneously.

This motivated us to search for other SSE materials with a better balance between ionic conductivity, deformability, and chemical and electrochemical stability from a refreshed perspective by comprehensively considering the valence state, ionic radius, polarizability, and electronegativity of anions. Compared to the divalent chalcogen anions, the monovalent halogen anions would have weaker Coulomb interactions with Li ions. On the other hand, ionic radii of halogen anions are larger than those of chalcogen anions ($r(Br^-)$ = 182 pm, $r(I^-)$ = 206 pm, $r(O^{2-})$ = 126 pm, and $r(S^{2-})$ = 170 pm for six-coordinated anions[14]), which lead to longer ionic bond length and higher anionic polarizability[15] and hence simultaneously enhance Li ionic conductivity and deformability. Moreover, halide materials usually show higher electrochemical oxidation and reduction stabilities, and better interfacial compatibilities with high-voltage $LiCoO_2$ cathode[16] than sulfides, which can be attributed to the higher electronegativity of halogen anions than that of sulfur anion. In the 1980s and 2000s, the spinel-structured halide materials with stable tetrahedral Li occupations were widely studied, such as $LiAlCl_4$,[17] Li_2MgCl_4,[18] and Li_2MgBr_4.[19] However, the advantages of

Received: May 27, 2019
Revised: August 14, 2019
Published: August 15, 2019

DOI: 10.1021/acs.chemmater.9b02075

halogen anions were not fully demonstrated in these spinel-structured halide materials, whose Li ion conductivities at room temperature are relatively small, on the order of 10^{-3} mS/cm or less. Recently, Asano et al. reported two new lithium halide solid-electrolyte materials, Li_3YCl_6 and Li_3YBr_6, with stable octahedral Li occupations, exhibiting a high Li ion conductivity of 1 mS/cm at room temperature, as well as high chemical and electrochemical stabilities.[16] Later, Mo et al. used first-principles simulations to investigate Li ion diffusion, electrochemical stability, and interface stability of these two recently reported Li_3YCl_6 and Li_3YBr_6 materials, and theoretically confirmed their high ionic conductivities and good electrochemical stabilities.[20] Hence, halide chemistry is a promising new research direction for developing future solid-state electrolytes with fast Li ion transports and good stabilities simultaneously. Meanwhile, a question that arises is that why the new Li_3YCl_6 and Li_3YBr_6 materials with stable octahedral Li occupations can achieve much higher ionic conductivities than the spinel structures with partial tetrahedral Li occupations, although they have similar close packed anion frameworks, e.g., face-centered-cubic (*fcc*) structures.

In this work, we investigated new nonspinel structured lithium ion conducting iodides with stable octahedral Li occupations, Li_3MI_6 (M = Sc, Y, and La), based on density functional theory (DFT) calculations. More importantly, the underlying mechanism for the superior Li ion transport in the nonspinel halides to that in the spinel ones was uncovered. Li_3LaI_6 is theoretically predicted to meet the requirements of high Li ionic conductivity, deformability, and chemical and electrochemical stability that sulfide-type SSEs alone have not completely achieved so far, which can be attributed to its long ionic bond length, high anionic polarizability, high stability of LaI_6^{3-} octahedra, and the beneficial Li conduction channel with considerable cation vacancy sites. Therefore, our iodide compound Li_3LaI_6 is quite promising to be utilized as a SSE material for lithium metal−iodine batteries and even ASSLIBs. Moreover, tuning the transition metal elements and strengthen the interactions between Li ion and the crystal lattice framework could effectively enhance Li ion diffusion in Li_3MI_6 with octahedral Li occupations. Such a design principle could be applied for searching new lithium, sodium, or multivalent ion superionic conductors.

2. COMPUTATIONAL METHODS

All calculations were performed using the Vienna *Ab*-initio simulation package (VASP) software, based on the projector-augmented wave method[21] within the framework of DFT.[22] The generalized gradient approximation (GGA)[23] in the form of Perdew−Burke−Ernzerhof exchange functional[22] was used. To consider the strong correlation effects of the transition metal in Li_3ScI_6, Li_3YI_6, and Li_3LaI_6 halides, both structural optimizations and electronic structure calculations were carried out using the spin-dependent GGA plus Hubbard correction U (GGA + U) method,[24] and the effective U_{eff} parameters were 5.00,[25] 3.00,[26] and 10.32 eV[27] for the Sc 3d, Y 4d, and La 4f states, respectively. The plane-wave energy cutoff was set to 520 eV. The Monkhorst−Pack method[28] with 3 × 2 × 1 and 6 × 4 × 2 k-point meshes was employed for the Brillouin zone sampling of Li_3MI_6 (M = Sc, Y, and La) unit cells, respectively, for structural relaxations and electronic structure calculations. The convergence criteria of energy and force were set to 10^{-5} eV/atom and 0.01 eV/Å, respectively.

The chemical and electrochemical stability of a material can be theoretically evaluated by the compositional phase diagram and lithium grand potential phase diagram,[29] respectively, constructed by the Pymatgen code based on the DFT ground-state energies of the corresponding compounds from the Materials Project open database.[30,31] Phonon calculations were carried out using the Cambridge Sequential Total Energy Package (CASTEP)[32] software based on the density functional perturbation theory.[33] The sets of the exchange functional, plane-wave energy cutoff, and k-mesh for CASTEP were the same as those for VASP. Activation energy barriers and diffusion coefficients of Li were calculated by the climbing image nudged elastic band (CI-NEB) method[34] and elevated-temperature *Ab*-initio molecular dynamics (AIMD) simulations.[35] A smaller plane-wave energy cutoff of 300 eV was chosen for AIMD simulations of the 2 × 1 × 1 Li_3MI_6 (M = Sc, Y, and La) supercells with a Gamma-centered 1 × 1 × 1 k-point grid. The time step was set to 2 fs, and all supercell systems were simulated for 20000 steps with a total time of 40 ps in a statistical ensemble with a fixed particle number, volume, and temperature (NVT). The charge analyses were performed by the Hirshfeld method[36] as implemented in- CASTEP software.

3. RESULTS AND DISCUSSION

3.1. Crystal Structure and Stability.

Our predicted monoclinic Li_3MI_6 (M = Sc, Y, and La) (in the C2 space group) have layered structures with O4 stacking patterns along the *c*-direction, denoted as O4-Li_3MI_6, where O represents MI_6 octahedra, and 4 represents the stacking sequences of ABCD for I anion layers, as shown in Figure 1. DFT-optimized lattice constants and atomic positions of the unit cells of Li_3MI_6 (M = Sc, Y, and La) are listed in Tables S1 and S2 in Supporting Information. The other two possible stacking sequences of Li_3MI_6 (M = Sc, Y, and La) were considered, including the O1 stacking of AA pattern (space group: $P2/m$) and the O2 stacking of ABAB pattern (space group: $C2/c$) (see Figure S1). DFT energies of O1-Li_3MI_6 (M = Sc, Y, and La) are slightly higher than those of O4 phases by 8.45, 8.61, and 8.27 meV/atom, respectively, and the corresponding energies of O2-Li_3MI_6 (M = Sc, Y, and La) are also slightly higher than those of O4 phases by 2.41, 2.60, and 2.44 meV/atom, respectively. Such small energy differences, much lower than the room-temperature k_BT of ∼26 meV/atom, indicate that O1, O2, and O4 structures are much likely to coexist in the experimentally synthesized Li_3MI_6 materials. To better understand the effects of the stacking sequences on Li ion diffusion, the slightly unstable O2-Li_3MI_6 (M = Sc, Y, and La) phases were also studied together with O4 phases.

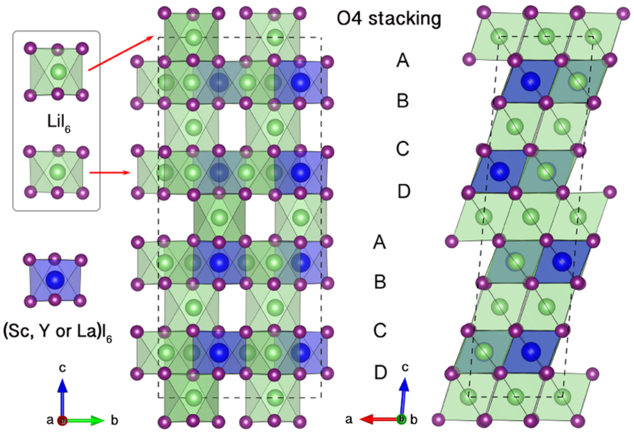

Figure 1. Unit cells of Li_3MI_6 (M = Sc, Y, and La) crystal with the O4 stacking sequences (LiI_6 octahedra in the transition metal layer and in the pure Li layer have different volumes). These crystal structure plots are displayed by the VESTA software.[37]

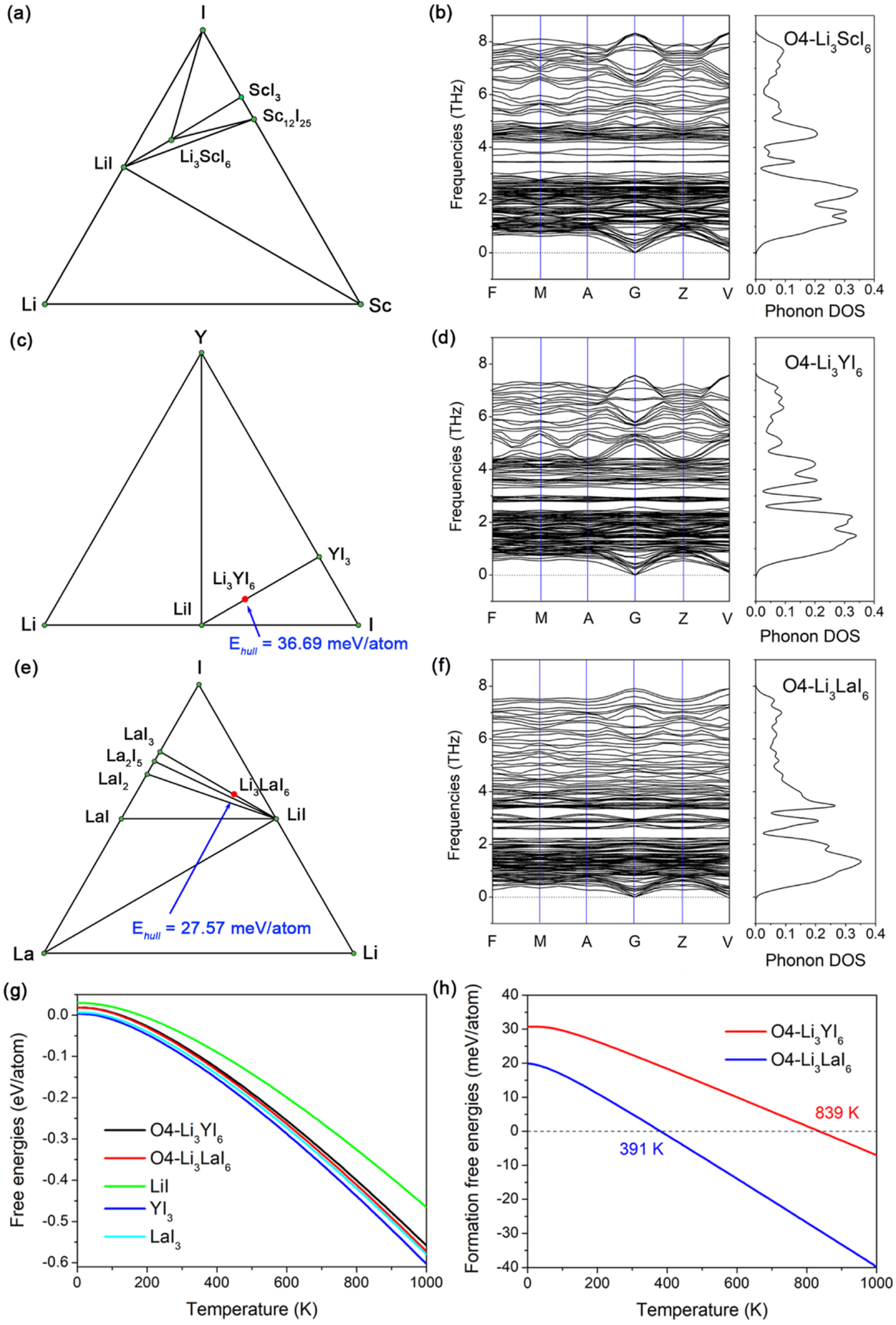

Figure 2. Thermodynamic and dynamic stabilities of O4-Li_3MI_6 (M = Sc, Y and La) materials. (a) DFT-calculated Li−Sc−I phase diagram; the green dots represent the stable compounds (O4-Li_3ScI_6 is stable in its ternary system), (c) DFT-calculated Li−Y−I phase diagram; O4-Li_3YI_6 phase is slightly higher in energy (energy above hull is 36.69 meV per atom) with respect to that of the ground-state mixtures of LiI and YI_3, (e) DFT-calculated Li−La−I phase diagram; O4-Li_3LaI_6 phase is slightly higher in energy (energy above hull is 27.57 meV per atom) with respect to that of the ground-state mixtures of LiI and LaI_3; (b), (d), and (f) phonon dispersions and total phonon density of states (DOS) of O4-Li_3ScI_6, O4-Li_3YI_6, and O4-Li_3LaI_6, respectively; (g) calculated temperature-dependent formation energies (Helmholtz free energies) of O4-Li_3YI_6 and O4-Li_3LaI_6 materials, and (h) Helmholtz free energies of O4-Li_3YI_6 and O4-Li_3LaI_6 as well as their equilibrium phases, LiI, YI_3, and LaI_3. O4-Li_3YI_6 and O4-Li_3LaI_6 are thermodynamically stable and can be entropically stabilized above 839 and 391 K, respectively.

Figures 1 and S1 show that there are 1/3 octahedral vacancy sites in the stoichiometric Li_3MI_6, benefitting Li ion diffusion. There are two kinds of stable Li occupation sites, namely, octahedral sites in the transition metal layer and in the pure lithium layer, respectively. These two kinds of LiI_6 octahedra have different volumes (different Li−I bond lengths), and the volumes of LiI_6 octahedra in the transition metal layer are slightly larger than those in the pure lithium layer. For the convenience of experimental structural characterization, the simulated X-ray diffraction pattern and calculated Raman spectra with characteristic vibration modes of O4- and O2-Li_3MI_6 (M = Sc, Y, and La) are provided in Figures S2 and S3.

The thermodynamic stabilities of Li_3MI_6 were specifically studied by constructing the Li−M−I ternary compositional

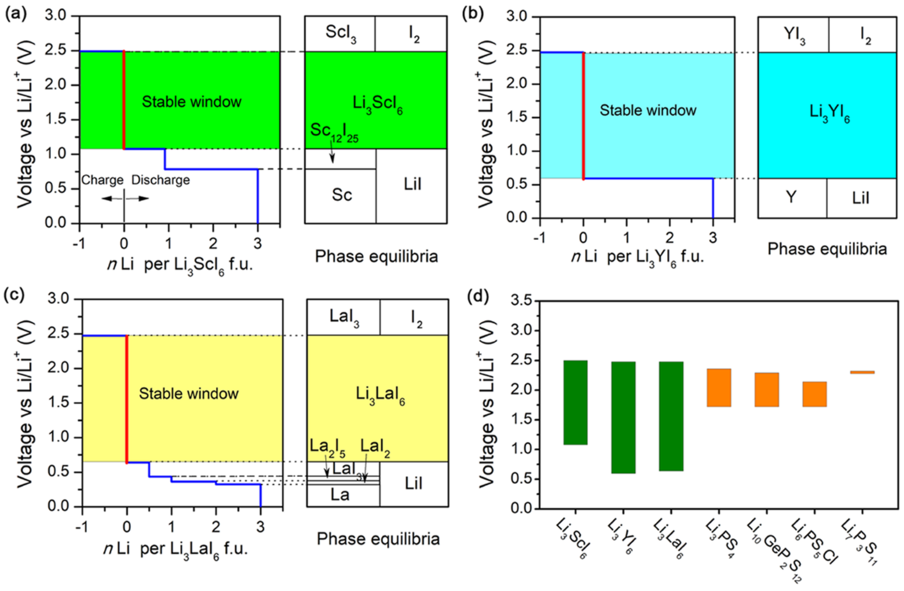

Figure 3. DFT-calculated voltage profiles (with respect to the chemical potential of Li metal) and phase equilibria of (a) O4-Li_3ScI_6, (b) O4-Li_3YI_6 and (c) O4-Li_3LaI_6 upon lithiation (Li metal insertion, $n > 0$) and delithiation (Li metal extraction, $n < 0$) based on the analyses of lithium grand potential phase diagrams, (d) DFT-calculated electrochemical windows of O4-Li_3MI_6 (M = Sc, Y, and La) iodides and other sulfide-type superionic conductors.

phase diagrams based on DFT-calculated energies[38]. Because O4- and O2-Li_3MI_6 phases have almost same DFT energies, here we only made thermodynamic stability analyses for O4-Li_3MI_6. A green dot in the DFT compositional phase diagrams (Figure 2) represents a stable compound whose energy is lower than that of any other compound at that composition. The Li−Sc−I phase diagram in Figure 2a shows that O4-Li_3ScI_6 phase is thermodynamically stable at 0 K with respect to its phase equilibrium compounds, LiI and ScI_3. We expect that the actual formation energy of Li_3ScI_6 at elevated temperatures could be even lower due to the entropic contributions. In addition, no imaginary vibrational mode is observed from the phonon dispersions of O4-Li_3ScI_6 (Figure 2b) and O2-Li_3ScI_6 (Figure S4a), indicating that both O4- and O2-Li_3ScI_6 are dynamically stable. Therefore, Li_3ScI_6 can be feasibly synthesized by the spontaneous reaction of its phase equilibrium compounds.

However, Figure 2c,e show that DFT energies of O4-Li_3YI_6 and O4-Li_3LaI_6 are slightly higher than those of the corresponding two-phase mixtures of LiI and YI_3 (LaI_3) by 36.69 and 27.57 meV/atom, respectively, which may be stabilized by the entropic contributions at elevated temperatures, such as lattice vibrational entropies. No imaginary vibrational mode is observed from the phonon dispersions of O4-Li_3YI_6, O4-Li_3LaI_6, O2-Li_3YI_6, and O2-Li_3LaI_6 (Figures 2d,f and S4b,c), which means that both Li_3YI_6 and Li_3LaI_6 are dynamically stable. By computing the lattice vibrational entropies of O4-Li_3YI_6, O4-Li_3LaI_6, YI_3, LaI_3, and LiI, the Helmholtz free energies as a function of temperature of these five compounds were obtained (Figure 2g). The formation free energies (E_f) of O4-Li_3MI_6 were calculated by E_f (O4-Li_3MI_6) = F(O4-Li_3MI_6) − 3F(LiI) − F(MI_3). The temperature-dependent E_f of O4-Li_3YI_6 and O4-Li_3LaI_6 are shown in Figure 2h, indicating that O4-Li_3YI_6 and O4-Li_3LaI_6 are entropically stabilized above 839 and 391 K, respectively. Similarly, O2-Li_3YI_6 or O2-Li_3LaI_6 might be more stable at higher temperatures than the O4 phases. Our formation energy calculations suggest that Li_3YI_6 and Li_3LaI_6 are stable at elevated temperatures. Moreover, the elastic constants of Li_3MI_6 (M = Sc, Y, and La) were calculated to verify their mechanical properties,[39] as summarized in Table S3. All of these elastic constants comply well with the Born criteria for a mechanically stable monoclinic crystal,[40,41] confirming the mechanical stabilities of Li_3MI_6. In addition, the elastic properties of electrolyte material are crucial parameters for designing SSLIBs.[42] A model proposed by Monroe et al. demonstrated that SSE materials with shear moduli twice that of lithium metal can effectively suppress the growth of lithium dendrites.[43] From the comparisons in Table S3, all calculated *B*, *E*, and *G* moduli of Li_3MI_6 are larger than twice that of Li metal,[40] suggesting that Li_3MI_6 would mechanically block the growth of lithium dendrites. Based on the above analyses of thermodynamic, dynamic, and mechanical stabilities, we can conclude that these three Li_3MI_6 (M = Sc, Y, and La) materials are much likely to be experimentally synthesized.

3.2. Electrochemical Stability.

The calculated band gaps of Li_3MI_6 (M = Sc, Y, and La) are in the range 2.86−3.58 eV, which can effectively insulate electron transport.[44] The element-projected band structures and density of states (Figure S5) show that the valence band maxima of Li_3MI_6 are dominated by I^- anion, which will be the first specie to be oxidized at high voltages. The conduction band minima of Li_3MI_6 are dominated by M^{3+} cation, which can be further reduced to M metal at low voltages. It is important to note that the band gap analyses only provide an upper limit of electrochemical stability.

During cycling operations of solid-state lithium batteries, the quite high lithium chemical potential at the anode side induces the reduction reactions of SSE materials with Li insertion, and the low lithium chemical potential (a strong oxidizing environment) at the charged cathode side would strongly oxidize SSEs with Li extraction.[29] Lithium grand potential phase diagrams, containing phase equilibrium with respect to the applied lithium potential,[38] were constructed to assess the electrochemical stabilities of O4-Li_3MI_6 (M = Sc, Y, and La). Because the construction of lithium grand potential phase

DOI: 10.1021/acs.chemmater.9b02075
Chem. Mater. 2019, 31, 7425−7433

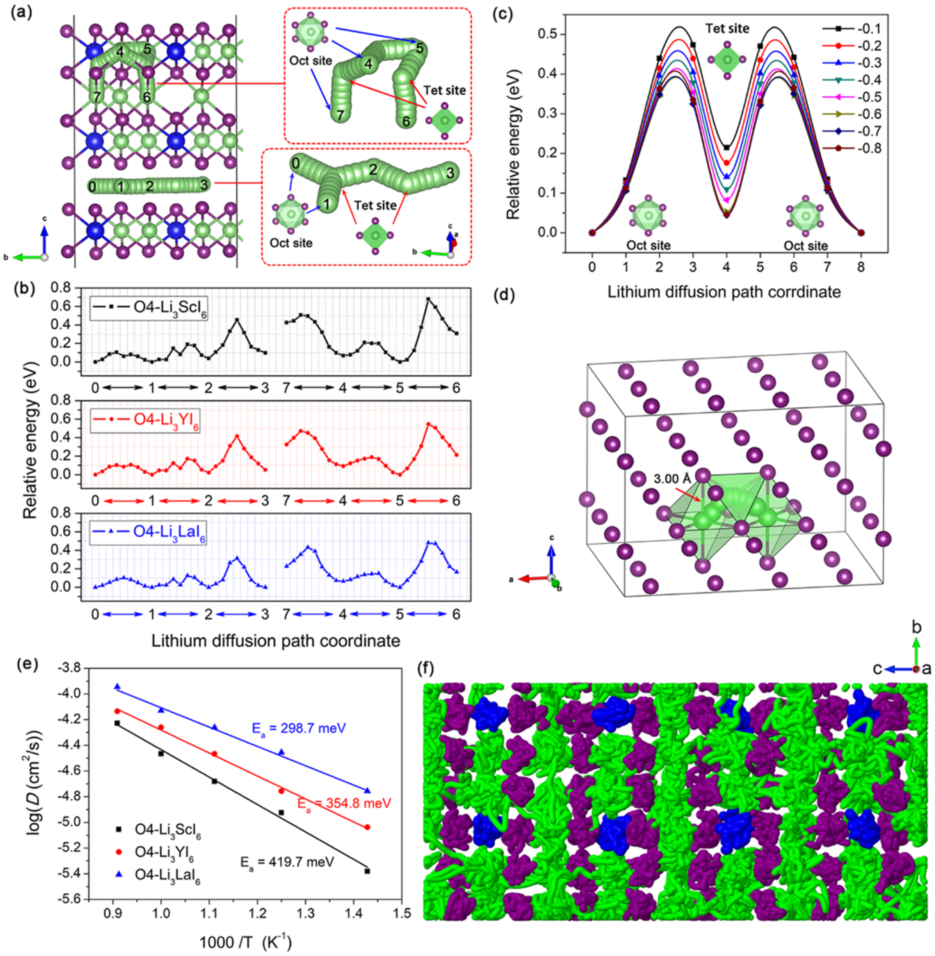

Figure 4. CI-NEB calculations and AIMD simulations for O4-Li_3MI_6 (M = Sc, Y, and La). (a) Seven different Li ion diffusion paths, including the intralayer paths (0 ↔ 1, 1 ↔ 2, 2 ↔ 3, and 4 ↔ 5) and crosslayer paths (4 ↔ 7 and 5 ↔ 6); the crystal structure plots are displayed using the VESTA software;[37] (b) energy variations of Li ion diffusion in O4-Li_3MI_6; (c) CI-NEB-calculated energy variations and (d) structural model of Li ion diffusion from one octahedral site to its adjacent octahedral site through a transition state with respect to different I anion charges in an *fcc* I sublattice with a single Li^+ ion (Li−I bond length in the octahedron is set to a constant of 3.00 Å). Only the migrating Li ion is allowed to relax whereas other anions are fixed; (e) Arrhenius plot of Li ion diffusion coefficient at different temperatures for O4-Li_3MI_6 (M = Sc, Y, and La); and (f) atomic trajectories from 900 K AIMD simulations of O4-Li_3LaI_6, displayed using the Jmol code,[46] where green, blue, and purple balls represent Li, La, and I atoms, respectively.

diagram is based on DFT energies, and O4- and O2-Li_3MI_6 phases have almost same DFT energies, we only focus on the relatively stable O4-Li_3MI_6 phases to represent Li_3MI_6 materials in the lithium grand potential phase diagram analyses. Based on the constructed lithium grand potential phase diagrams of the Li−M−I ternary systems, we obtained DFT-calculated voltage profiles and phase equilibria of O4-Li_3MI_6 (M = Sc, Y, and La) upon lithiation and delithiation, as depicted in Figure 3. From Figure 3a, when the voltage is higher than 2.49 V, the active I^- anion in Li_3ScI_6 will be oxidized to I_2 and the ScI_3 phase with Li extraction. However, Li_3ScI_6 begins to be lithiated at 1.08 V, and decomposes into LiI and the $Sc_{12}I_{25}$ phase. When the voltage is further decreased to 0.784 V, the formed $Sc_{12}I_{25}$ begins to be further reduced to Sc metal and LiI upon lithiation. Therefore, the calculated electrochemical window of Li_3ScI_6 is from 1.08 to 2.49 V, with a window width of 1.41 V. Similar redox reactions can also be found for O4-Li_3YI_6 and Li_3LaI_6 (Figure 3b,c). The electrochemical windows of Li_3YI_6 and Li_3LaI_6 are 1.93 and 1.83 V, ranging from 0.55 to 2.48 V and from 0.64 to 2.47 V, respectively. Figure 3d shows that the electrochemical window widths of Li_3MI_6 (M = Sc, Y, and La) iodides are much larger than those (0.10−0.75 V) of sulfides, indicating that Li_3MI_6 iodides have much higher electrochemical stabilities and better compatibilities with electrodes than sulfides, especially their antireduction stabilities. The above electrochemical stability analyses are from the perspective of the thermodynamic driving force for decomposition reaction. However, the kinetic factors, including the morphology, electronic and ionic conductivity of the decomposition products, and the applied current, are very important in determining the extent of decomposition reaction,[8] which were not considered here. We believe the formed electronically insulating but ionically conducting interphases of Li_3MI_6 (M = Sc, Y, and La) (see details in the Supporting Information) can effectively extend their electrochemical stability windows by the limited kinetics of decomposition reaction.

3.3. Lithium Ion Diffusivity and Conductivity. A high ionic conductivity of 10^{-3}−10^{-2} S/cm at room temperature is the first requirement for the application of ionic conductors as SSEs for ASSLIBs. In this section, Li ion diffusivities and conductivities of Li_3MI_6 were investigated by the CI-NEB calculations and AIMD simulations.[45] Li ion diffusion in Li_3MI_6 is mainly based on the vacancy diffusion mechanism, due to the abundant octahedral vacancy sites in the stoichiometric Li_3MI_6 unit cells (Figures 1 and S1). Because O4-Li_3MI_6 iodides have different Li occupation environments, we considered five different paths for Li ion diffusion from one octahedron site to its adjacent octahedron site through a transition state, as shown in Figure 4a, including the intralayer paths (0 ↔ 1, 1 ↔ 2, 2 ↔ 3, and 4 ↔ 5) and crosslayer paths (4 ↔ 7 and 5 ↔ 6). The calculated energy variations of Li ion diffusion in O4-Li_3MI_6 (M = Sc, Y, and La) by the CI-NEB method are shown in Figure 4b, and the corresponding energy barriers for different diffusion paths are listed in Table S5. The activation energy barriers of the crosslayer paths are relatively higher than those of the intralayer paths, indicating that Li ion diffusion within the $x-y$ plane is slightly easier than that along the z-direction. Overall, the activation energy barriers of Li ion diffusion along each path in O4-Li_3MI_6 (M = Sc, Y, and La) follow the order of $Li_3ScI_6 > Li_3YI_6 > Li_3LaI_6$, indicating that the heavier the transition metal M (with the same valence state), the easier the Li ion diffusion in O4-Li_3MI_6.

Recent works on superionic conductors have demonstrated the influence of lattice dynamic that softer lattices would lead to lower activation barriers for ion diffusion. In other words, fast lithium ion conductors usually show low lithium vibration frequencies or low center of lithium phonon density of states (DOS).[47] Here, we have also calculated the partial phonon density of states of Li atom in O4- and O2-Li_3MI_6 (M = Sc, Y, and La) and obtained their corresponding phonon DOS centers, as shown in Figure S7. For both O4- and O2-Li_3MI_6, the phonon DOS centers follow the trend of $Li_3LaI_6 < Li_3YI_6 < Li_3ScI_6$, which is fully consistent with the order of bulk moduli in Table S3 and the activation energy barriers from CI-NEB calculations. In addition, the phonon band centers of O4-Li_3MI_6 (M = Sc, Y, and La) are slightly lower than those of O2-types, in accordance with the bulk moduli of O4-types being smaller than those of O2-types in Table S3.

Considering that the activation energy barriers from the CI-NEB calculations are diffusion-path-dependent, CI-NEB calculations cannot provide the total activation energy barrier as experiments. Therefore, we performed AIMD simulations to further understand Li ion diffusion in Li_3MI_6 and obtain the total activation energy barriers. Figures 4e and S8 show the Arrhenius plots of Li ion diffusion coefficients at different elevated temperatures of O4- and O2-Li_3MI_6 (M = Sc, Y, and La), respectively. The overall activation energy barriers of Li ion diffusion in O4-Li_3MI_6 (M = Sc, Y, and La) are calculated to be 419.7, 354.8, and 298.7 meV, respectively (Table S6). In addition, the overall Li diffusion activation energy barriers of O2-Li_3MI_6 (M = Sc, Y, and La) are 426.3, 372.2, and 305.5 meV, respectively. The extrapolated Li ion diffusion coefficients at 300 K of O4-Li_3MI_6 (M = Sc, Y, and La) are 3.84×10^{-10}, 3.51×10^{-9}, and 2.40×10^{-8} cm^2/s, respectively, and the corresponding ionic conductivities are 0.02, 0.19, and 1.23 mS/cm, respectively (Table S6). And Li ion diffusion coefficients at 300 K of O2-Li_3MI_6 (M = Sc, Y, and La) are 4.40×10^{-10}, 2.43×10^{-9}, and 1.94×10^{-8} cm^2/s, respectively, and the corresponding ionic conductivities are 0.03, 0.13, and 0.99 mS/cm, respectively. It can be seen that O4-Li_3MI_6 have slightly higher extrapolated ionic conductivities than O2-types at room temperature. The room-temperature ionic conductivities of 0.99−1.23 mS/cm of Li_3LaI_6 are comparable to those of the state-of-the-art sulfide-type solid electrolytes, such as LGPS and LPS. The atomic trajectories in Figure 4f show that the steady I anion frameworks are well maintained, and no breaking of M−I bonds is observed during the entire 900 K AIMD simulations. Moreover, the mean-square-displacement (MSD) data (Figure S9) and atomic trajectories of Li (Figure S10) clearly exhibit significant three-dimensional (3D) Li hopping. The CI-NEB calculations and AIMD simulations demonstrate that Li_3LaI_6 is a 3D superionic conductor, which meets the first requirement of high ionic conductivity of 10^{-3}–10^{-2} S/cm at room temperature and is highly promising to be utilized as a SSE material.

3.4. Influence of Anionic Charge on Lithium Ion Diffusion. Usually, the measured activation energy barrier (E_a) is the sum ($E_a = \Delta H_m + 0.5H_f$) of the migration enthalpy change (ΔH_m) and the defect formation enthalpy (H_f).[48,49] In a lithium superionic conductor, the Li defect formation enthalpy is often negligibly small, and the measured E_a can be approximated by ΔH_m value.[49] Furthermore, according to our previous research studies on the chalcopyrite-structured $LiMS_2$ (M represents 3d transition metals from Sc to Ni),[50] the charge and bond length dependent Coulombic interactions between Li cation and its adjacent S anions significantly affect Li ion diffusion. To better understand the lithium diffusion mechanism in the nonspinel Li_3MI_6, where I atoms form an *fcc* sublattice and Li atoms occupy the octahedral central sites, we studied the correlation of E_a *vs* the potential difference (E_p) between the tetrahedral central site (transition state, E_{tet}) surrounded by four I anions and its adjacent octahedral central site (equilibrium state, E_{oct}) surrounded by six I anions in an *fcc* I anion sublattice model, which allows us to directly assess the effects of anion.[51] Since the octahedral centers are the stable Li occupation sites in our nonspinel Li_3MI_6 ($E_{tet} > E_{oct}$ or $E_p > 0$), a smaller E_p leads to a smaller H_m (Figure S11). The total potential of a reference positive ion, interacting with all other anions in an *fcc* I anion sublattice, approximately equals the sum of the non-electrostatic potential and the total electrostatic potential of all Li−I pairs. Therefore, we obtained

$$E_a \approx \Delta H_m \propto E_p = E_{tet} - E_{oct} \approx \left[C_1 - \sum_{i=1}^{n} \frac{e^2|q_I|}{4\pi\epsilon d_i}\right] - \left[C_2 - \sum_{j=1}^{n} \frac{e^2|q_I|}{4\pi\epsilon d_j}\right] \approx C - \frac{e^2}{4\pi\epsilon}\left[\sum_{i=1}^{n}\frac{1}{d_i} - \sum_{j=1}^{n}\frac{1}{d_j}\right] \times |q_I| \approx C - \frac{Ae^2}{4\pi\epsilon}\left(\frac{|q_I|}{d_{oct}}\right)$$

, where the reference ion of Li is assumed to have one charge e, C_1 and C_2 are the non-electrostatic potentials, ϵ is the dielectric constant, q_I is the charge of an I anion, d_i are the distances between the tetrahedral Li site and its ith-neighbor I anions, d_j are the distances between the octahedral Li site and its jth-neighbor I anions, C is a positive constant ($C = C_1 - C_2$); $\left[\sum_{i=1}^{n}\frac{1}{d_i} - \sum_{j=1}^{n}\frac{1}{d_j}\right]$ is convergent to a positive constant A/d_{oct}, as shown in Figure S12, and d_{oct} is the distance between the octahedral Li site and its first nearest-neighbor I anion. It can be seen that the larger values of $|q_I|/d_{oct}$ result in smaller E_p, consequently reducing E_a for the octahedral Li ion diffusion.

In contrast, for Li ion diffusion in the spinel halides usually from one tetrahedral equilibrium site to another tetrahedral equilibrium site through an octahedral transition state, we can obtain $E_a \propto E_{oct} - E_{tet} \approx C' + \frac{Ae^2}{4\pi\epsilon}\left(\frac{|q_{anion}|}{d_{tet}}\right)$, where C' is a positive constant, q_{anion} is the charge of the anion, and d_{tet} is the distance between the tetrahedral central site and its first nearest-neighbor anion. It can be clearly found that the larger values of $|q_{anion}|/d_{tet}$ give rise to an increase in E_p, leading to higher E_a for the tetrahedral Li ion diffusion. For the spinel-structured $LiAlCl_4$, Li_2MgCl_4, and Li_2MgBr_4, the very active Mg and Al elements with smaller ionic radii correspond to larger $|q_{Cl}|/d_{tet}$ and $|q_{Br}|/d_{tet}$ ratios, eventually resulting in higher E_a and poor ionic conductivities. This similar effect can also be found in $Li_{10}MP_2S_{12}$ (M = Ge and Sn) with stable tetrahedral Li occupations. The lower electronegativity of Sn *vs* Ge (10.2 *vs* 11.1)[52] gives rise to more electrons on S anions in $Li_{10}SnP_2S_{12}$,[53] leading to the larger $|q_S|/d$ value, as shown in Table S7, and thereby increases its E_a compared to those of $Li_{10}GeP_2S_{12}$, which are in good accordance with AIMD simulations by Ong et al.[54]

The atomic Hirshfeld charges and Li−I bond lengths of Li_3MI_6 were calculated, as shown in Table S8 and Figure S13, respectively. Atomic Hirshfeld charges indicate that the charges of I anion for both O4- and O2-structures slightly increase from Li_3ScI_6 to Li_3LaI_6. This is because La atom is the most active one among the elements of group IIIB (Sc (χ_A = 7.0) > Y (χ_A = 6.3) > La (χ_A = 6.0)[52]), which can donate more electrons to its adjacent I anions. The Gaussian distributions of Li−I bond lengths show that the average bond lengths are 3.00, 3.03, and 3.06 Å for O4-Li_3MI_6 (M = Sc, Y, and La), respectively, and 3.05, 3.06, and 3.08 Å for O2-Li_3MI_6 (M = Sc, Y, and La), respectively. Although the Li−I bond lengths of Li_3LaI_6 are slightly larger than those of Li_3MI_6 (M = Sc and Y), the $|q_I|/d_{oct}$ value of Li_3LaI_6 is still the largest, and the $|q_I|/d_{oct}$ values follow the order of $Li_3LaI_6 > Li_3YI_6 > Li_3ScI_6$ (Figure 5), which is consistent with the sequences of anion charge. Hence, the anion charges play more crucial roles in determining the $|q_I|/d_{oct}$ values than the Li−I bond length (bottleneck areas, Table S6) in Li_3MI_6 materials. This larger $|q_I|/d_{oct}$ value of Li_3LaI_6 would result in the lower phonon DOS center of Li, corresponding to the smaller E_p between LiI_4 tetrahedra and LiI_6 octahedra and hence the lower E_a for Li ion diffusion. The recently reported Li_3YCl_6 and Li_3YBr_6 superionic conductors with stable octahedral Li occupations also show relatively larger $|q_{Cl}|/d_{oct}$ and $|q_{Br}|/d_{oct}$ ratios (Figure 5), and this may be why ion transport in these new nonspinel structures is superior to that in the spinel-structured halides with tetrahedral Li occupations, although they have the same *fcc* anion frameworks. In addition, the $|q_{Cl}|/d_{oct}$ value of Li_3YCl_6 is larger than the $|q_{Br}|/d_{oct}$ value of Li_3YBr_6, making the activation barrier of Li_3YCl_6 lower than that of Li_3YBr_6, which is consistent with the results from 500 K AIMD simulations by Mo et al.[20]

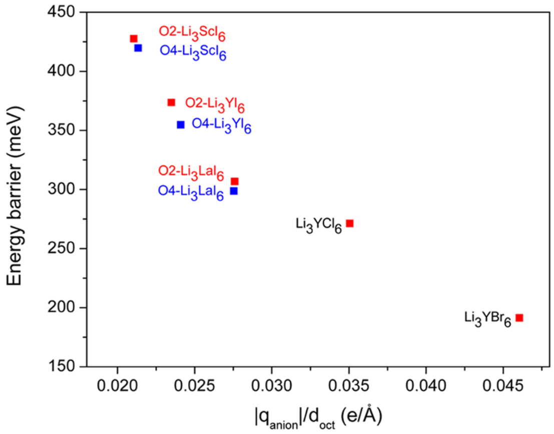

Figure 5. $|q_{anion}|/d_{oct}$-dependent activation energy barriers for Li ion diffusion in O4-Li_3MI_6, O2-Li_3MI_6 (M = Sc, Y, and La), Li_3YCl_6, and Li_3YBr_6, respectively, where Li takes octahedral sites.

To further verify the anion charge dependent E_p, we have monitored the energy variations (Figure 4c) of Li ion diffusion from one octahedral site to its adjacent octahedral site through a transition state with respect to different I anion charges in a *fcc* I sublattice, in which only one migrating Li^+ ion was considered (Figure 4d). This similar calculation method can also be found in the previous work by Ceder et al.[51] Figure 4c shows that E_p between LiI_4 tetrahedron and LiI_6 octahedron decreases with the increase of I anion charge, resulting in a lower E_a for the system with more negatively charged anions. Therefore, we can conclude that the electronegativity of M element has a fundamental impact on Li ion diffusion in Li_3MI_6, and the smaller electronegativity of La atoms makes faster Li ion diffusion in Li_3LaI_6.

Here, based on the profound understandings of Li_3MI_6 and other reported superionic conductors, we identified an alternative design principle for searching new ternary lithium superionic conductors with octahedral occupations, which can also be applied to sodium or multivalent ion superionic conductors. The large electronegativity difference between the anion element and non-lithium cation element leading to large $|q_{anion}|/d_{oct}$ values is essential for achieving extremely fast lithium ion diffusion in a superionic conductor with Li octahedral occupations, as depicted in Figure 5, and the corresponding non-lithium cation element M should locate at the left bottom of the periodic table with a small electronegativity and a large atomic number.

4. CONCLUSIONS

In this work, Li_3LaI_6 with stable octahedral Li occupations is theoretically found to simultaneously meet the requirements of high lithium ionic conductivity, deformability, and chemical and electrochemical stability that sulfide-type SSEs alone have not completely achieved so far. Our DFT calculations demonstrate that Li_3LaI_6 superionic conductor is promising to be experimentally synthesized and utilized as a solid-state electrolyte material for all-solid-state lithium ion batteries with a wider electrochemical window than that of sulfides and high ionic conductivities of 1.23−2.08 mS/cm, comparable to those of the state-of-the-art sulfide-type solid electrolytes, such as $Li_{10}GeP_2S_{12}$ and Li_3PS_4. The underlying mechanism of superior Li ion conduction in such halide superionic conductors with stable octahedral Li occupations compared to the spinel ones with tetrahedral Li occupations has been uncovered. A relationship between the migration enthalpy and anion charge for those materials with face-centered-cubic anion frameworks has been identified: (1) a large $|q_{anion}|/d_{oct}$ ratio favors Li ion hopping between the equilibrium octahedral sites through tetrahedral transition site; (2) a small $|q_{anion}|/d_{tet}$ ratio is beneficial to the Li diffusion between tetrahedral sites through octahedral transition sites. Such a design principle could be applied for searching new lithium, sodium, or multivalent ion superionic conductors. For example, in a ternary lithium ion conductor with stable Li octahedral occupations, a larger electronegativity difference between the anion element and non-lithium cation element is essential to obtain large $|q_{anion}|/d_{oct}$ ratios and hence to enhance lithium-ion conductivity.

■ ASSOCIATED CONTENT

Supporting Information

The Supporting Information is available free of charge on the ACS Publications website at DOI: 10.1021/acs.chemmater.9b02075.

> Structural information; phonon dispersions and DOS; elastic constants and elastic properties; electronic structures; electrochemical stability against electrodes; Li ion diffusion properties; total and direction projected MSD; atomic trajectories of AIMD simulations; atomic Hirshfeld charges (PDF)

■ AUTHOR INFORMATION

Corresponding Author

*E-mail: hong.zhu@sjtu.edu.cn.

ORCID

Hong Zhu: 0000-0001-7919-5661

Notes

The authors declare no competing financial interest.

■ ACKNOWLEDGMENTS

This work was supported by the National Natural Science Foundation of China (51602196), Shanghai Automotive Industry Corporation (1714), and Materials Genome Initiative Center at Shanghai Jiao Tong University. All simulations were performed at the Shanghai Jiao Tong University High Performance Computing Center.

■ REFERENCES

(1) Zhang, Z.; Shao, Y.; Lotsch, B.; Hu, Y.-S.; Li, H.; Janek, J.; Nazar, L. F.; Nan, C.-W.; Maier, J.; Armand, M.; Chen, L. New horizons for inorganic solid state ion conductors. *Energy Environ. Sci.* **2018**, *11*, 1945−1976.

(2) Judez, X.; Chunmei, L.; Rodriguez-Martinez, L. M.; Zhang, H.; Eshetu, G. G.; Armand, M. Opportunities for Rechargeable Solid-State Batteries Based on Li-Intercalation Cathodes. *Joule* **2018**, *2*, 2208−2224.

(3) Sun, C.; Liu, J.; Gong, Y.; Wilkinson, D. P.; Zhang, J. Recent advances in all-solid-state rechargeable lithium batteries. *Nano Energy* **2017**, *33*, 363−386.

(4) Kamaya, N.; Homma, K.; Yamakawa, Y.; Hirayama, M.; Kanno, R.; Yonemura, M.; Kamiyama, T.; Kato, Y.; Hama, S.; Kawamoto, K.; Mitsui, A. A lithium superionic conductor. *Nat. Mater.* **2011**, *10*, 682−686.

(5) Phuc, N. H. H.; Totani, M.; Morikawa, K.; Muto, H.; Matsuda, A. Preparation of Li_3PS_4 solid electrolyte using ethyl acetate as synthetic medium. *Solid State Ionics* **2016**, *288*, 240−243.

(6) Xie, H.; Alonso, J. A.; Li, Y.; Fernández-Díaz, M. T.; Goodenough, J. B. Lithium Distribution in Aluminum-Free Cubic $Li_7La_3Zr_2O_{12}$. *Chem. Mater.* **2011**, *23*, 3587−3589.

(7) Morimoto, H.; Awano, H.; Terashima, J.; Shindo, Y.; Nakanishi, S.; Ito, N.; Ishikawa, K.; Tobishima, S.-i. Preparation of lithium ion conducting solid electrolyte of NASICON-type $Li_{1+x}Al_xTi_{2-x}(PO_4)_3$ (x = 0.3) obtained by using the mechanochemical method and its application as surface modification materials of $LiCoO_2$ cathode for lithium cell. *J. Power Sources* **2013**, *240*, 636−643.

(8) Han, F.; Zhu, Y.; He, X.; Mo, Y.; Wang, C. Electrochemical Stability of $Li_{10}GeP_2S_{12}$ and $Li_7La_3Zr_2O_{12}$ Solid Electrolytes. *Adv. Energy Mater.* **2016**, *6*, No. 1501590.

(9) Xu, L.; Tang, S.; Cheng, Y.; Wang, K.; Liang, J.; Liu, C.; Cao, Y.-C.; Wei, F.; Mai, L. Interfaces in Solid-State Lithium Batteries. *Joule* **2018**, *2*, 1991−2015.

(10) Zhang, W.; Richter, F. H.; Culver, S. P.; Leichtweiss, T.; Lozano, J. G.; Dietrich, C.; Bruce, P. G.; Zeier, W. G.; Janek, J. Degradation Mechanisms at the $Li_{10}GeP_2S_{12}/LiCoO_2$ Cathode Interface in an All-Solid-State Lithium-Ion Battery. *ACS Appl. Mater. Interfaces* **2018**, *10*, 22226−22236.

(11) Zhu, Y.; He, X.; Mo, Y. First principles study on electrochemical and chemical stability of solid electrolyte−electrode interfaces in all-solid-state Li-ion batteries. *J. Mater. Chem. A* **2016**, *4*, 3253−3266.

(12) Thompson, T.; Yu, S.; Williams, L.; Schmidt, R. D.; Garcia-Mendez, R.; Wolfenstine, J.; Allen, J. L.; Kioupakis, E.; Siegel, D. J.; Sakamoto, J. Electrochemical Window of the Li-Ion Solid Electrolyte $Li_7La_3Zr_2O_{12}$. *ACS Energy Lett.* **2017**, *2*, 462−468.

(13) Manthiram, A.; Yu, X.; Wang, S. Lithium battery chemistries enabled by solid-state electrolytes. *Nat. Rev. Mater.* **2017**, *2*, No. 16103.

(14) Shannon, R. D. Revised effective ionic radii and systematic studies of interatomic distances in halides and chalcogenides. *Acta Crystallogr., Sect. A: Cryst. Phys., Diffr., Theor. Gen. Crystallogr.* **1976**, *32*, 751−767.

(15) Ashcroft, N. W.; Mermin, N. D. *Solid State Physics*; Holt, Rinehart and Winston: New York, 1976; pp 533−559.

(16) Asano, T.; Sakai, A.; Ouchi, S.; Sakaida, M.; Miyazaki, A.; Hasegawa, S. Solid Halide Electrolytes with High Lithium-Ion Conductivity for Application in 4 V Class Bulk-Type All-Solid-State Batteries. *Adv. Mater.* **2018**, *30*, No. 1803075.

(17) Weppner, W. Ionic Conductivity of Solid and Liquid $LiAlCl_4$. *J. Electrochem. Soc.* **1977**, *124*, 35.

(18) Nagel, R.; Gro, T. W.; Günther, H.; Lutz, H. D. 6Li and 7Li MAS NMR Studies on Fast Ionic Conducting Spinel-Type Li_2MgCl_4, $Li_{2-x}Cu_xMgCl_4$, $Li_{2-x}Na_xMgCl_4$, and Li_2ZnCl_4. *J. Solid State Chem.* **2002**, *165*, 303−311.

(19) Kanno, R. Ionic Conductivity and Phase Transition of the Bromide Spinels, $Li_{2-2x}M_{1+x}Br_4$(M = Mg, Mn). *J. Electrochem. Soc.* **1986**, *133*, 1052.

(20) Wang, S.; Bai, Q.; Nolan, A. M.; Liu, Y.; Gong, S.; Sun, Q.; Mo, Y. Lithium Chlorides and Bromides as Promising Solid-State Chemistries for Fast Ion Conductors with Good Electrochemical Stability. *Angew. Chem., Int. Ed.* **2019**, *58*, 8039−8043.

(21) Blöchl, P. E. Projector augmented-wave method. *Phys. Rev. B: Condens. Matter Mater. Phys.* **1994**, *50*, 17953−17979.

(22) Kohn, W.; Sham, L. J. Self-Consistent Equations Including Exchange and Correlation Effects. *Phys. Rev* **1965**, *140*, A1133−A1138.

(23) Perdew, J. P.; Burke, K.; Ernzerhof, M. Generalized Gradient Approximation Made Simple. *Phys. Rev. Lett.* **1996**, *77*, 3865−3868.

(24) Dudarev, S. L.; Botton, G. A.; Savrasov, S. Y.; Humphreys, C. J.; Sutton, A. P. Electron-energy-loss spectra and the structural stability of nickel oxide: An LSDA+U study. *Phys. Rev. B* **1998**, *57*, 1505−1509.

(25) Meng, Q.; Enzuo, L.; Xinbin, M.; Qingfeng, G.; Jinlong, G.; Gong, J.; Wang, T. Understanding electronic and optical properties of anatase TiO_2 photocatalysts co-doped with nitrogen and transition metals. *Phys. Chem. Chem. Phys* **2013**, *15*, 9549−9561.

(26) Stevanović, V.; Lany, S.; Zhang, X.; Zunger, A. Correcting density functional theory for accurate predictions of compound enthalpies of formation: Fitted elemental-phase reference energies. *Phys. Rev. B* **2012**, *85*, No. 115104.

(27) Wu, D.; Prange, M. P.; Gao, F.; Kerisit, S. First-principles search for efficient activators for LaI_3. *J. Lumin.* **2016**, *176*, 227−234.

(28) Monkhorst, H. J.; Pack, J. D. Special points for Brillouin-zone integrations. *Phys. Rev. B* **1976**, *13*, 5188−5192.

(29) Deng, Z.; Zhu, Z.; Chu, I.-H.; Ong, S. P. Data-Driven First-Principles Methods for the Study and Design of Alkali Superionic Conductors. *Chem. Mater.* **2017**, *29*, 281−288.

(30) Ong, S. P.; Richards, W. D.; Jain, A.; Hautier, G.; Kocher, M.; Cholia, S.; Gunter, D.; Chevrier, V. L.; Persson, K. A.; Ceder, G. Python Materials Genomics (pymatgen): A robust, open-source python library for materials analysis. *Comput. Mater. Sci.* **2013**, *68*, 314−319.

(31) Jain, A.; Ong, S. P.; Hautier, G.; Chen, W.; Richards, W. D.; Dacek, S.; Cholia, S.; Gunter, D.; Skinner, D.; Ceder, G.; Persson, K. A. Commentary: The Materials Project: A materials genome approach to accelerating materials innovation. *APL Mater.* **2013**, *1*, No. 170901.

(32) Clark, S. J.; Segall, M. D.; Pickard, C. J.; Hasnip, P. J.; Probert, M. I. J.; Refson, K.; Payne, M. C. First principles methods using CASTEP. *Z. Kristallogr. - Cryst. Mater.* **2005**, *220*, 567−570.

(33) Baroni, S.; de Gironcoli, S.; Dal Corso, A.; Giannozzi, P. Phonons and related crystal properties from density-functional perturbation theory. *Rev. Mod. Phys.* **2001**, *73*, 515−562.

(34) Henkelman, G.; Jónsson, H. Improved tangent estimate in the nudged elastic band method for finding minimum energy paths and saddle points. *J. Chem. Phys.* **2000**, *113*, 9978−9985.

(35) Zhu, Z.; Chu, I.-H.; Ong, S. P. $Li_3Y(PS_4)_2$ and $Li_5PS_4Cl_2$: New Lithium Superionic Conductors Predicted from Silver Thiophosphates using Efficiently Tiered Ab Initio Molecular Dynamics Simulations. *Chem. Mater.* **2017**, *29*, 2474−2484.

(36) Fonseca Guerra, C.; Handgraaf, J.-W.; Baerends, E. J.; Bickelhaupt, F. M. Voronoi deformation density (VDD) charges: Assessment of the Mulliken, Bader, Hirshfeld, Weinhold, and VDD methods for charge analysis. *J. Comput. Chem.* **2004**, *25*, 189−210.

(37) Momma, K.; Izumi, F. VESTA 3 for three-dimensional visualization of crystal, volumetric and morphology data. *J. Appl. Crystallogr.* **2011**, *44*, 1272−1276.

(38) Ong, S. P.; Wang, L.; Kang, B.; Ceder, G. Li−Fe−P−O_2 Phase Diagram from First Principles Calculations. *Chem. Mater.* **2008**, *20*, 1798−1807.

(39) Liu, C. S.; Zhu, H. H.; Ye, X. J.; Yan, X. H. Prediction of a new BeC monolayer with perfectly planar tetracoordinate carbons. *Nanoscale* **2017**, *9*, 5854−5858.

(40) Mouhat, F.; Coudert, F.-X. Necessary and sufficient elastic stability conditions in various crystal systems. *Phys. Rev. B* **2014**, *90*, No. 224104.

(41) Born, M.; Huang, K. *Dynamic Theory of Crystal Lattice*; Clarendon: Oxford, 1954.

(42) Deng, Z.; Wang, Z.; Chu, I.-H.; Luo, J.; Ong, S. P. Elastic Properties of Alkali Superionic Conductor Electrolytes from First Principles Calculations. *J. Electrochem. Soc.* **2016**, *163*, A67−A74.

(43) Monroe, C.; Newman, J. The Impact of Elastic Deformation on Deposition Kinetics at Lithium/Polymer Interfaces. *J. Electrochem. Soc.* **2005**, *152*, A396−A404.

(44) Goodenough, J. B.; Kim, Y. Challenges for Rechargeable Li Batteries. *Chem. Mater.* **2010**, *22*, 587−603.

(45) Ceder, G.; Ong, S. P.; Wang, Y. Predictive modeling and design rules for solid electrolytes. *MRS Bull.* **2018**, *43*, 746−751.

(46) Hanson, R. M. Jmol−a paradigm shift in crystallographic visualization. *J. Appl. Crystallogr.* **2010**, *43*, 1250−1260.

(47) Muy, S.; Bachman, J. C.; Giordano, L.; Chang, H.-H.; Abernathy, D. L.; Bansal, D.; Delaire, O.; Hori, S.; Kanno, R.; Maglia, F.; Lupart, S.; Lamp, P.; Shao-Horn, Y. Tuning mobility and stability of lithium ion conductors based on lattice dynamics. *Energy Environ. Sci.* **2018**, *11*, 850−859.

(48) Culver, S. P.; Koerver, R.; Krauskopf, T.; Zeier, W. G. Designing Ionic Conductors: The Interplay between Structural Phenomena and Interfaces in Thiophosphate-Based Solid-State Batteries. *Chem. Mater.* **2018**, *30*, 4179−4192.

(49) Krauskopf, T.; Muy, S.; Culver, S. P.; Ohno, S.; Delaire, O.; Shao-Horn, Y.; Zeier, W. G. Comparing the Descriptors for Investigating the Influence of Lattice Dynamics on Ionic Transport Using the Superionic Conductor $Na_3PS_{4-x}Se_x$. *J. Am. Chem. Soc.* **2018**, *140*, 14464−14473.

(50) Xu, Z. M.; Bo, S. H.; Zhu, H. $LiCrS_2$ and $LiMnS_2$ Cathodes with Extraordinary Mixed Electron-Ion Conductivities and Favorable Interfacial Compatibilities with Sulfide Electrolyte. *ACS Appl. Mater. Interfaces* **2018**, *10*, 36941−36953.

(51) Wang, Y.; Richards, W. D.; Ong, S. P.; Miara, L. J.; Kim, J. C.; Mo, Y.; Ceder, G. Design principles for solid-state lithium superionic conductors. *Nat. Mater.* **2015**, *14*, 1026.

(52) Rahm, M.; Zeng, T.; Hoffmann, R. Electronegativity Seen as the Ground-State Average Valence Electron Binding Energy. *J. Am. Chem. Soc.* **2019**, *141*, 342−351.

(53) Krauskopf, T.; Culver, S. P.; Zeier, W. G. Bottleneck of Diffusion and Inductive Effects in $Li_{10}Ge_{1-x}Sn_xP_2S_{12}$. *Chem. Mater.* **2018**, *30*, 1791−1798.

(54) Ong, S. P.; Mo, Y.; Richards, W. D.; Miara, L.; Lee, H. S.; Ceder, G. Phase stability, electrochemical stability and ionic conductivity of the $Li_{10\pm1}MP_2X_{12}$ (M = Ge, Si, Sn, Al or P, and X = O, S or Se) family of superionic conductors. *Energy Environ. Sci.* **2013**, *6*, 148−156.

DOI: 10.1021/acs.chemmater.9b02075
Chem. Mater. 2019, 31, 7425−7433